Title

Effect of exercise on patient specific abdominal aortic aneurysm flow topology and mixing

Permalink

https://escholarship.org/uc/item/3j4387sp

Journal

International Journal for Numerical Methods in Biomedical Engineering, 30(2)

ISSN

2040-7939

Authors

Arzani, Amirhossein
Les, Andrea S
Dalman, Ronald L
et al.

Publication Date

2014-02-01

DOI

10.1002/cnm.2601

Peer reviewed

Effect of exercise on patient specific abdominal aortic aneurysm flow topology and mixing

Amirhossein Arzani[1], **Andrea S. Les**[2], **Ronald L. Dalman**[3], and **Shawn C. Shadden**[1,*]

[1]Mechanical Engineering, University of California, Berkeley, CA, USA

[2]Bioengineering, Stanford University, Stanford, CA, USA

[3]Division of Vascular Surgery, Stanford University, Stanford, CA, USA

SUMMARY

Computational fluid dynamics modeling was used to investigate changes in blood transport topology between rest and exercise conditions in five patient-specific abdominal aortic aneurysm models. Magnetic resonance imaging was used to provide the vascular anatomy and necessary boundary conditions for simulating blood velocity and pressure fields inside each model. Finite-time Lyapunov exponent fields, and associated Lagrangian coherent structures, were computed from blood velocity data, and used to compare features of the transport topology between rest and exercise both mechanistically and qualitatively. A mix-norm and mix-variance measure based on fresh blood distribution throughout the aneurysm over time were implemented to quantitatively compare mixing between rest and exercise. Exercise conditions resulted in higher and more uniform mixing, and reduced the overall residence time in all aneurysms. Separated regions of recirculating flow were commonly observed in rest, and these regions were either reduced or removed by attached and unidirectional flow during exercise, or replaced with regional chaotic and transiently turbulent mixing, or persisted and even extended during exercise. The main factor that dictated the change in flow topology from rest to exercise was the behavior of the jet of blood penetrating into the aneurysm during systole.

Keywords

Computational fluid dynamics; hemodynamics; transport; Lagrangian coherent structures

---

1. INTRODUCTION

An abdominal aortic aneurysm (AAA) is a localized enlargement of the abdominal aorta that accompanies disturbed blood flow, which is thought to perpetuate aneurysm progression. Rupture of AAA is one of the leading causes of death for the elderly in the United States, and an exact intervention decision for this disease has always been associated with uncertainty. AAA diameter, along with patient history, is the common parameter for surgical decision, nevertheless rupture of smaller AAA is known to occur.

There is currently no pharmaceutical treatment of AAA, and lower extremity exercise is a proposed therapy that may favorably affect the mechanisms behind the initiation and progression of AAA [1, 2]. Higher risk of AAA has been demonstrated in persons that suffer from reduced infrarenal abdominal aortic blood flow, including persons with spinal cord

*Correspondence to: S. C. Shadden, 5121 Etcheverry Hall, Berkeley, CA, 94720-1740., shadden@berkeley.edu.

injury [3], and persons with above-knee amputation [4]. Increased flow rates in the abdominal aorta associated with lower limb exercise appears to protect against atherosclerosis formation [5], which is one of the risk factors for AAA development [6]. In addition, reduced retrograde flow, higher mean wall shear stress, lower oscillatory shear index (OSI), and a decreased diastolic length resulting from exercise [7, 8] may be beneficial in preventing or slowing AAA.

Different studies have investigated the effect of exercise on AAA flow and stress fields. Idealized models have been used to compare rest and exercise conditions in AAA, including the transition to turbulence and vortex formation [9], the effect of wall compliance [10], and pressure and wall shear stress (WSS) changes [11]. More recently patient specific modeling has been used to provide closer representations of *in vivo* conditions. Les et al. [12] compared WSS, OSI, and turbulent kinetic energy between different patient specific AAA models during rest and exercise. Suh et al. [13] compared the particle residence time (PRT) between different patients at mild and moderate exercise intensities.

The present study seeks to compare the topology of blood transport and mixing in patient specific AAAs during rest and exercise. For the purpose of studying blood flow topology, the computation of finite-time Lyapunov exponent (FTLE) fields and Lagrangian coherent structures (LCS) has been used [14, 15]. This approach uncovers various features of unsteady chaotic flows that are not obtained from traditional Eulerian characterizations of blood flow. For a quantitative comparison of mixing we propose a method with mix-norm and mix-variance measures [16]. In section 2 the modeling and post-processing methods are described in more detail. The results of these analyses are presented in section 3 and discussed in section 4.

2. METHODS

Five patients with small AAA (diameter <5 cm) having distinct morphologies were chosen for this study. Velocity data was obtained by image-based computational fluid dynamics (CFD), with magnetic resonance imaging (MRI) providing the computational domain and data for boundary conditions. The resulting velocity data was used in FTLE/LCS, and mixing quantification, calculations.

2.1. Image Based Computational Fluid Dynamics

Imaging studies were conducted under a protocol approved by the institutional review board and informed consent was obtained from all participants. Contrast-enhanced magnetic resonance angiography (MRA) was used to obtain images of the abdominal aorta and the surrounding arteries. A modified version of the software package *SimVascular* [17] was used for reconstructing arterial lumina. Each model started from the level of the diaphragm and included the supraceliac aorta, celiac trunk (hepatic and splenic arteries), superior mesenteric artery (SMA), the renal arteries, and the internal and external iliac arteries. The reconstructed geometries represented the blood flow domain and thus accounted for any boundaries due to the arterial wall, or mural thrombus as may have been present.

The models were used as computational domains to solve the Navier-Stokes equations using a stabilized finite element method [18, 19]. Volumetric flow rates over time through the supraceliac and infrarenal aorta were derived from flow sensitive 2D phase contrast (PC) MRI measurements in each patient during the time of the scan. The supraceliac flow rate waveform was mapped to a Womersley profile and imposed at the inlet face of the model as a Dirchelet boundary condition. While it is unlikely that flow in the descending thoracic aorta has an axisymmetric Womersley profile, the inlet was chosen to be relatively far from the region of interest (aneurysm) so that idealizations introduced at this location would have

minimal influence. Along the vessel wall, a zero velocity (no-slip) condition was prescribed. At the model outlets, three element Windkessel (RCR) models were used to represent the downstream vasculature beds [20]. The total resistance ($R_{tot} = R_d + R_p$) at each outlet was determined from dividing the mean brachial pressure measured for each patient by the expected mean flow to the outlet. Expected mean flow rates to the aortic branch arteries were determined from first differencing the measured infrarenal and supraceliac flow rates. This difference was subsequently distributed 33.0% to the celiac trunk and the remaining 67% equally among the SMA, left renal artery, and the right renal artery. Infrarenal flow was split equally between iliac arteries, and subsequently 70% of common iliac flow was distributed to the external iliac and 30% to the internal iliac [21]. The resistance ratio R_p/R_{tot} was assumed to be 5.6%, except for the renal arteries where it was set to 28% to ensure anterograde diastolic flow. The total arterial capacitance was obtained by the pulse pressure method [22] using measured systolic and diastolic blood pressures, and distributed to each outlet proportional to its expected flow rate.

Moderate lower limb exercise waveforms were derived from the resting waveforms by methods described in [12]. Briefly, a roughly 5-fold increase in infrarenal flow and 20% decrease in flow to the abdominal branches was imposed, resulting in roughly a 2.5-fold increase in supraceliac flow depending on the patient. Diastole was shortened so that the resting heart rate was increased by 50%, and the resulting waveform was shifted to match the new supraceliac mean. This waveform was mapped to a Womerseley profile and imposed at the inlet. Figure 1 displays the rest and exercise waveforms. The exercise waveforms, and pressures derived from data in [23], were used to compute new values for total resistance and arterial compliance, which were distributed similarly as done for rest, except the proximal resistance (R_p) was kept the same as rest, and the distal resistance (R_d) was adjusted accordingly.

Each model was meshed using linear tetrahedral finite elements with maximum edge size of 500 microns. This resulted in an average mesh size of around 10 million elements, as based on the mesh independence study in [12], which compared results from ≈2M, ≈8M and ≈32M element meshes to confirm that results showed minor grid dependence at the ≈8M element mesh size. Simulations were run until the solution appeared sufficiently converged (periodicity of the pressure waves were obtained), and five subsequent cardiac cycles of the resulting velocity data were used for postprocessing computations. Table I shows the Reynolds number at the infrarenal level for each patient at peak systole during rest and exercise.

2.2. FTLE/LCS Computations

The velocity field data from image-based CFD provides instantaneous flow field information. When viewed directly, these data or other instantaneous measures derived from them, do not typically shed much insight into blood transport. That is, the chaotic nature of fluid trajectories is often not recognizable from inspection of instantaneous rate of change information. However, the velocity data can be used to solve directly for the trajectories of fluid element. Resulting trajectory data is highly complex in most realistic flows and the computation of Lagrangian coherent structures provides a framework to uncover the underlying templates of fluid trajectory motion [24]. Namely, turning points in the flow due to vortical structures, flow separation, or flow attachment result in partitionings of the flow that are uncovered by LCS.

A relatively robust and straightforward method to identify LCS is by the computation of finite time Lyapunov exponent fields, and extracting LCS as hypersurfaces that locally maximize the FTLE measure [25, 26]. In order to compute FTLE, a grid of fluid elements

(massless tracers) in the region of interest are advected by the velocity field v(x, t) obtained by CFD, i.e. the positions of tracers are obtained from the advection equation

$$\dot{\mathbf{x}}(t) = \mathbf{v}(\mathbf{x}, t) \quad (1)$$

over a grid of initial conditions $\{x(t_0)\}$. The flow map

$$\phi_{t_0}^{t+\tau} : \mathbf{x}(t_0) \mapsto \mathbf{x}(t_0 + \tau), \quad (2)$$

is computed at each initial condition by integration of Eq. (1) with an integration time τ. The FTLE is then computed at each location as [25]:

$$\mathbf{\Lambda}(\mathbf{x}, t_0, \tau) = \frac{1}{|\tau|} \ln \|D\phi_{t_0}^{t+\tau}\|_2, \quad (3)$$

where $\|.\|_2$ is the induced 2-norm. The *repelling* LCS were extracted from the FTLE field computed using a positive integration time ($\tau > 0$), whereas the *attracting* LCS were obtained by integration backward in time ($\tau < 0$). The integration time was set to the cardiac cycle length T for each case, which is typically a suitable choice for cardiovascular applications [14]. The $1/|\tau|$ factor was dropped in the FTLE definition (Eq. 3) in order to prevent spurious FTLE values that occur when tracers leave the computational domain in a short time. The FTLE field was computed every 1/25th of the cardiac cycle (i.e., $t_0 = i\, T/25$ for $i = 0, \ldots, 24$) to evaluate the time evolution of the LCS.

2.3. Quantification of Mixing

LCS help to reveal the mechanisms of advective transport. However, to quantify mixing via a single measure a metric is needed. In order to quantify mixing we follow the definitions of mix-norm and mix-variance in [16], and propose a suitable scalar field to be used for these measures. The key idea of mix-norm is to integrate the square of the averaged values of the given field over a set of sub-domains, instead of the whole space, so that mixing over all scales can be assessed.

To understand mixing, we evaluate how new blood penetrating into the aneurysm occupies the aneurysm as compared to the blood that is initially inside the aneurysm. That is, two sets of dense tracers that follow the fluid are introduced. First, tracers are seeded to initially occupy the entire aneurysm at $t = 0$ (*initial tracers*). These tracers are released only once. Second, tracers are constantly released based on the flow rate at the inlet of the aneurysm (*inlet tracers*). These tracers are released at all times. A scalar function c is defined as the percentage of inlet tracers on a volumetric basis, Eq. (4).

Let Γ be the domain of interest (the aneurysm in this case). The aneurysm is divided into distinct equally-spaced subdomains $\Gamma_i(s_j)$, such that

$$\Gamma = \bigcup_{i=1}^{N_{s_j}} \Gamma_i(S_j),$$

where N_{s_j} is the total number of subdomains, and s_j is the particular length scale used to form the subdomains. The function $c_i(s_j, t)$ in domain $\Gamma_i(s_j)$, and at time t is obtained by

$$c_i(s_j,t) = \frac{\sum\limits_{\mathrm{x}(t)\in\Gamma_i(s_j)} \mathrm{inlet\ \ tracers}}{\left(\sum\limits_{\mathrm{x}(t)\in\Gamma_i(s_j)} \mathrm{initial\ \ tracers}\right) + \left(\sum\limits_{\mathrm{x}(t)\in\Gamma_i(s_j)} \mathrm{inlet\ \ tracers}\right)}, \quad (4)$$

where $\mathrm{x}(t)$ is the tracer position given by Eq. (1). Therefore, c_i is the percentage of inlet tracers in subdomain Γ_i, which is a function of time and the size s_j of Γ_i. A metric is developed to measure c over the domain

$$\varphi(c,s_j,t) = \left(\frac{1}{N_{s_j}}\sum_{i=1}^{N_{s_j}} c_i(s_j,t)^2\right)^{\frac{1}{2}}. \quad (5)$$

Subsequently the mix-norm is defined by further developing a metric to measure c over all choices of length scales s_j

$$\Phi(c,t) = \left(\frac{1}{N_t}\sum_{j=1}^{N_t} \varphi(c,s_j,t)^2\right)^{\frac{1}{2}}, \quad (6)$$

where N_t is the total number of length scales used ($s_j j = 1, \ldots, N_t$). The mix-norm quantifies the ratio of "new blood" to "old blood" in a way that is invariant of location or scale. Our goal is to observe how Φ changes over time in each AAA between rest and exercise.

In order to quantify variations of the amount of mixing throughout the domain we compute the mix-variance. To define mix-variance, the mixing in the entire domain is evaluated by replacing $\Gamma_i(s_j)$ in Eq. (4) with Γ. Denoting the resulting function as $c(\bar{t})$, the mix-variance is

$$\Phi^2(c - \bar{c}, t) = \frac{1}{N_t}\sum_{j=1}^{N_t} \varphi(c - \bar{c}, s_j, t)^2. \quad (7)$$

The above procedure was repeated for each 1/25th of the cardiac cycle, and for a total of five cardiac cycles. The tracer initial positions were seeded with a uniform spacing of 1 mm in each direction. A total of five different length scales ($N_t = 5$) were used in mix-norm calculations. These scales divided the aneurysm to 2^3, 4^3, 6^3, 8^3, 10^3 number of subdomains in each case.

Residence time was also computed to evaluate stasis. The PRT is calculated as the minimum time needed for a tracer at position x_0 at time t to leave the domain Γ, i.e.,

$$PRT(\mathbf{x}_0, t; \Gamma) = \min(t') \in (0, \infty)\mathrm{s.\ \ t.\ \ } x(\mathbf{x}_0, t+t') \notin \Gamma. \quad (8)$$

The PRT was calculated for five cardiac cycles, with the same spatial resolution of the tracer seeding used for mix-norm calculations. Regions of high residence time are thought to play an important role in the formation of thrombus due to low particle clearance that can lead to platelet aggregation [27]. To quantify the overall level of PRT for each case, a mix-norm for particle residence time was calculated ($\Phi(PRT(\mathrm{x}_0, t; \Gamma))$), based on the method described above.

In performing Lagrangian post processing, tracers may cross no-slip boundaries (vessel wall) due to the discrete nature of integration. This can lead to errors in Lagrangian based measures if not properly handled. As discussed in prior publications [28, 29], an efficient, yet accurate, method to solve this problem is to impose a very small inward velocity at the no-slip nodes along the vessel walls that effectively negates or reverses a particle's outward normal velocity component (as may be expected for when a cell or other particle collides with the vessel wall). The imposed inward velocity is typically set such that the local CFL condition is at least 3 orders of magnitude less than 1; i. e., a very small but finite inward velocity is needed to prevent leakage due to truncation errors. Using this method helped ensure, in an accurate manner, that particles only leave the fluid domain through model outlets, as expected.

3. RESULTS

Figure 2 displays the computational models, and the sagittal cross-sections used for displaying the FTLE results. The following figures show the backward and forward FTLE fields at different phases of the cardiac cycle for the five patients. The colorbars are scaled to the maximum range of each case accordingly. It should be noted that the FTLE fields were derived from full 3D computations, however a cross-section of these fields have been chosen to simplify visualization.

3.1. Changes to Flow Topology from Rest to Exercise

Patient 1—Figure 3 displays the FTLE fields for Patient 1. The prominent region of low backward FTLE in the left two columns indicates a coherent penetrating jet during both rest and exercise. Flow separation and vortical structures along the posterior wall during rest are mostly reduced or removed by the penetrating jet in exercise. However, exercise appears to contribute to furthering flow separation on the anterior wall. Specifically, under resting conditions there is a prominent separation bubble that forms in the upper anterior aspect of the aneurysm during systole due to the sudden expansion of the anterior wall. Furthermore, the penetrating systolic jet rolls up into a large laminar vortex ring, which is fully developed and most clearly observed during mid-deceleration (1st column, middle row). Therefore, two sources of recirculation are present in the anterior bulge; one is from the core of the vortex ring, and the other from the separation bubble. Both regions are bound by prominent LCS during mid-deceleration. Under exercise conditions, the jet does not appear to roll up into a vortex ring but instead the increased flow results in relatively unidirectional flow through the innermost region of the aneurysm. However, flow separation at the proximal, anterior wall of the aneurysm clearly persists, and roll-up associated with this separation is observed during peak systole (2nd column, top row). Under resting conditions, the impingement and break up of the large systolic vortex ring leads to mixing due to large scale vortices throughout the aneurysm during diastole (1st column, bottom row). However, this is not the case under exercise. The unidirectional flow through the innermost regions results in the anterior bulge remaining relatively cut off from the penetrating inflow throughout the cardiac cycle. The fluid in this separated region does eventually mix over several cardiac cycles with the blood pumping through the aneurysm, but this occurs through entrainment and detrainment mechanisms into and out of the recirculation regions, not a complete washout of the recirculation zone. For this patient, exercise never removes, or even reduces, separated recirculating flow in the anterior bulge.

Patient 2—Figure 4 displays the FTLE fields for Patient 2. Under resting conditions flow into the aneurysm rolls up into a vortex ring, which is indicated by the low FTLE values in the proximal segment during peak systole (1st column, top row). Immediately distal to this vortex is highly chaotic flow, as indicated by the region of high backward FTLE. This

disorganization to the flow appears to quickly destabilize the vortex, which leads to break up in the proximal segment during deceleration. Under exercise conditions, the systolic jet is able to penetrate slightly farther into the main aneurysm bulge. The jet appears to lack the strength or coherence to penetrate through the aneurysm, which is contrary to what was observed for Patient 1. During rest the *proximal* breakdown of the jet creates highly chaotic flow in the proximal aneurysm during diastole (1st column, bottom row). However, the deeper penetration of the jet prior to breakdown during exercise leads to significantly higher chaotic mixing in the *distal* segment (2nd column, bottom row) under increased flow conditions. Unlike Patient 1, the highly recirculatory flow was not confined to a specific region, but instead occupied most of the aneurysm. The prominent flow separation (aLCS1) and subsequent recirculation region formed on the posterior wall of the main bulge during rest conditions appeared to be removed by the highly chaotic mixing during exercise. Differences in the forward FTLE fields are also dramatic. Under resting conditions, larger scale, laminar vortical structures dominate the flow topology in the aneurysm. Under exercise conditions, there is lack of coherent flow features and small scale mixing is observed over the entire aneurysm in the forward FTLE field. This indicates that as blood passes through the aneurysm it becomes well mixed before reaching the iliac bifurcation.

Patient 3—Figure 5 displays the FTLE fields for Patient 3. This patient had noticeable left-to-right curvature of the abdominal aorta. Under resting conditions, the systolic jet forms a weak and shortly lived vortex ring, and the flow topology during rest appears mainly dominated by large scale vortices and laminar flow conditions. During exercise, the backward FTLE fields indicate that the flow into the aneurysm is coherent. However, under exercise the inflow does break up in the distal portion of the aneurysm, leading to highly chaotic flow in the distal segment (2nd column, bottom row). The influence of this mixing in the distal segment to the flow through the aneurysm is apparent in the forward FTLE fields. Under rest, the forward FTLE fields indicate mild mixing as blood passes through the aneurysm. During exercise, the forward FTLE indicates vigorous and small scale mixing as blood passes through the aneurysm, and this occurs throughout the entire aneurysm domain.

Patient 4—Figure 6 displays the FTLE fields for Patient 4. Under resting conditions, a systolic vortex ring is formed from the jet of blood into the aneurysm during systole. Similar to Patient 2, the vortex breaks up in the proximal segment, however for this patient the break up of the vortex appears to result from impingement of leading edge of the vortex (aLCS1) on the anterior wall (1st column, middle row). This leads to more highly disturbed flow conditions in the proximal than distal segment of the aneurysm. Indeed, the forward FTLE fields during rest showed very little change in the distal segment of the aneurysm as well. Similar to previous patients, the inflow into the aneurysm under exercise conditions does not lead to a coherent vortex ring. Also similar to Patient 2, the flow here penetrates deeper into the aneurysm during exercise, but eventually breaks up leading to disturbed flow conditions in the distal segment during exercise, instead of the proximal segment as for rest. The backward FTLE reveals the appearance of extended separation lines in exercise, that is the separation lines in rest (aLCS2) are not removed by the jet in exercise, but instead the separation boundary (aLCS3) appears to have become extended. This separation on the posterior wall appears to contribute to the systolic vortex during rest, and systolic jet during exercise, being directed to the anterior wall, which prevents inflow from coherently penetrating into the aneurysm, even though the abdominal aorta is relatively straight and the aneurysm is diffuse. Similarly to Patient 3, blood moving through the aneurysm is not well mixed during rest, but becomes more highly mixed during exercise. Nonetheless, comparing the spacing and density of the structures in the forward and backward FTLE fields under exercise conditions with those from other patients, it is clear that less small scale mixing may be observed for this patient during exercise.

Patient 5—Figure 7 displays the FTLE fields for Patient 5. This patient has a highly tortuous abdominal aorta and complex bi-lobed aneurysm shape. This led to a lack of coherent flow features and mostly chaotic flow topology throughout much of the abdominal aorta under resting conditions. While exercise led to slight stabilization of the inflow jet, the overall flow topology did not change significantly for this patient. That is, mild turbulence dominated the flow in this aneurysm under both rest and exercise.

Integration Time—To observe the effect of integration time τ in the computation of the FTLE fields, different choices of τ are plotted for the first patient in Fig. 8. Many of the prominent LCS are revealed even for short integration times. Comparing the FTLE fields in the forth and fifth column demonstrates that there is little change to the actual structures revealed. Hence, increasing the integration time beyond the cardiac length typically does not introduce new LCS or significant changes to description of the flow topology. This is also in large part because after one cardiac cycle, most tracers have been flushed from the computational domain and hence are no longer being tracked and therefore will not contribute to changing the FTLE.

Mixing—Figures 9 and 10 show the mix-norm and mix-variance results, respectively, for all patients. The domain Γ in these computations was the aneurysm bulge. That is, quantification of mixing was made over the aneurysm itself, not the entire model. Based on the definition of the scalar function in Eq.(4), the rate that the mix-norm approaches unity can be considered a metric for comparison of mixing rates among the patients. Exercise led to improvement of mixing in the aneurysm for all patients. As expected from the FTLE/LCS results, Patient 4 had the lowest mixing. The mix-variance results show the amount of variation that mixing has in the subdomains of an aneurysm as compared to the overall mixing in the entire aneurysm quantified by the mixed norm. It can be seen from Fig. 10 that mix-variance is reduced during exercise, i.e., a more uniform mixing occurs throughout the aneurysm. Figure 11 shows the mix-norm residence time results. The residence time reduces noticeably during exercise. Patient 4, and Patient 5 had the highest and lowest residence time respectively, during both rest and exercise.

PCMRI Comparison—Velocity fields obtained from CFD were compared with velocity fields obtained by PCMRI at the mid-aneurysm level. Results of this comparison for Patient 2 are shown in Fig. 12. Both the computational results and PCMRI measurements show significant swirling/vortices at the mid-aneurysm level with qualitatively similar spatial features and velocity magnitudes. This indicates that the flow features at the mid-aneurysm level seem largely induced by the geometry modeled, rather than the inlet boundary profile. The differences between the PCMRI and CFD velocity fields are multifactorial including modeling assumptions used in generating CFD flow data, and cycle to cycle averaging and various filtering required in generating PCMRI flow data. Reproducibility studies of PCMRI measurements show differences similar to differences between the PCMRI and CFD results obtained herein, therefore the CFD results are expected to reasonably reproduce in vivo flow conditions inside the AAA.

4. DISCUSSION

Changes to flow topology from rest to exercise in patient specific AAAs has been studied. This is one of the first studies to carefully examine transport in AAA during exercise, a challenging task due to the enhanced chaotic and transiently turbulent flow features that occur under these conditions. Our results demonstrate that prominent large scale flow features generally observed during rest are removed in most, but not all, cases during exercise.

The main factor that determined the changes to the flow topology in exercise was the behavior of the penetrating jet in systole. It was previously observed that the evolution of the systolic vortex determined the flow topology in AAA under resting conditions [15], and in a similar way the dynamics of the penetrating jet during exercise strongly influences the flow topology in AAA under exercise conditions. The jet either washed away recirculating regions that occurred under resting conditions, leaving regions of high local mixing near the walls, or the breakdown of the jet replaced recirculation regions with regions of chaotic mixing connected throughout the entire aneurysm. Finally, the penetrating flow could in some cases add to the extent of the separated flow regions.

The regions of high forward and backward FTLE observed throughout much of the aneurysms in exercise, and during rest in some cases, represent regions of closely spaced LCS that cause enhanced mixing of the flow. These regions are referred to as chaotic due to this implied topology. While defining when a flow is chaotic is a delicate task [30], chaotic flows are generally governed by homoclinic and heteroclinic tangles of invariant manifolds between hyperbolic sets [31]. These tangles gives rise to complex phase space transport typically described as chaos. LCS can reveal analogous invariant manifolds, and indeed the regions observed as having high FTLE were regions of dense heteroclinic tangles of LCS. The dynamics of these structures lead to complex mixing and high sensitivity to initial conditions, which are referred to as chaotic. It should be noted that these regions contain in fact high and low FTLE values, but appear as regions of high FTLE when viewed macroscopically.

Regions of dense LCS can be associated with small scale vortices from the presence of mild turbulence [32], thus we often consider regions of dense LCS are both chaotic and transiently turbulent. However, one must take care in considering the finite-time nature of the FTLE computation to properly interpret such regions. An example is the creation of a localized region of high FTLE such as confined to the anterior wall of the aneurysm in Patient 1 during exercise. While mild levels of turbulent kinetic energy exists in much of the aneurysm during exercise, the blood inside this anterior "pocket" is mostly cut off from the systolic jet passing through the aneurysm and the blood outside this region is flushed from the domain relatively quickly. The blood inside the high FTLE region is not necessarily confined to this region and it eventually mixes with the rest of the domain during diastole, but in doing so the blood spreads over time throughout the domain resulting in further stretching and hence higher FTLE (i.e., further resolved structures) as the integration time increases. This is apparent in Fig. 8, especially during exercise conditions (bottom row). The FTLE field along the proximal anterior wall corresponds to blood in, or entrained to, a region of separated, recirculating flow. The FTLE field continues to progress in this region as the integration time is increased, however the FTLE in the rest of the domain remains relatively unchanged since blood originating in this regions has been flushed.

The increased flow rates associated with exercise increases the Reynolds number, and subsequently the levels of turbulence intensity. The transitional behavior of the flow might question the usefulness of LCS in interpretation of transport. More specifically, the relative importance of advective mixing versus diffusive mixing is usually considered to answer this question. The domination of diffusion in quasi-turbulent flows usually does not eliminate the advective patterns, and the LCS remain in the flow for considerable time [33]. In the present study a method was presented for direct quantification of mixing based on the fresh blood that occupies the aneurysm. The results based on this method are consistent with the interpretation of mixing from the LCS results. However, both of these methods are based on advection, and the interaction between advective and diffusive mixing contribute to the overall mixing in the aneurysm.

Several prior image-based computational studies of AAA hemodynamics have placed the inlet boundary condition in the abdominal aorta, and in doing so often neglected the major abdominal branch arteries. Under this scenario the flow in the aneurysm becomes sensitive to the chosen inlet velocity profile [34]. Moreover, disturbances due to flow separation from the celiac, superior mesenteric and renal ostia, as well as induced retrograde flow in the infrarenal aorta from the presence of these branch arteries, is not properly modeled. In this study the inlet boundary condition was imposed at the descending thoracic aorta. This, along with direct modeling of the major branch arteries proximal to the aneurysm, helped to ensure that idealization of the inlet profile would have minimal influence to flow topology in the aneurysm. As shown in Fig. 12, even though the computational results used an axisymmetric Womersley inlet profile, the vortical and swirling motions at the mid-aneurysm level were consistent with PCMRI measurement, indicating that flow topology was largely induced by the geometry, rather than the inlet boundary profile. This finding is consistent with prior results of Tang, et al., [8] who found little difference in abdominal aortic WSS and OSI patterns when prescribing either a Womersley inlet profile, or a measured inlet profile obtained by PCMRI at the supraceliac level.

The flow topology may be influenced by the idealized rigid wall, and Newtonian rheology assumptions. The effect of the rigid wall assumption has been shown recently to have relatively minor influence to Lagrangian measures of blood flow through a total cavopulmonary connection application [29]. Since typical deformation of AAA are of similar magnitude, we expect that fluid-structure interactions will not significantly alter the main flow features observed in this study. The effect of blood rheology on vortex formation inside AAA has been studied previously [35]. While some change to the flow topology was demonstrated, it remains unclear whether changes due to expected variations in blood rheology are significant in comparison to cycle to cycle variations in the flow and potential inaccuracies in boundary conditions (including errors in lumen reconstruction) [36].

We have proposed a method to compare the overall particle residence time inside aneurysms quantitatively. Residence time is hypothesized to be correlated with thrombosis. Furthermore, higher mixing inside AAA is thought to be beneficial. However, it is not clear that poor mixing is adverse. Indeed, unidirectional flow leads to poor mixing and this is the preferred physiologic state. Patient 3, followed by Patient 4, exhibited the most significant increase in chaotic mixing from rest to exercise. Although the backward FTLE shows that exercise is washing away some of the disturbed regions in rest, the sparse LCS in the forward FTLE during rest shows that the bulk of the flow is unidirectional. This questions whether the high mixing observed in exercise is beneficial for these patients. Nonetheless, in locations of recirculating flow, increased mixing is likely beneficial. Therefore, the ratio $\Phi(PRT, t)/\Phi(c, t)$ may be considered as a parameter to correlate these advective properties of the flow to the likelihood of thrombosis. However, there are many factors that can lead to the formation of thrombus, and these parameters are only based on transport mechanisms.

There are several hemodynamic parameters in AAA that are affected by lower extremity exercise [12, 13]. Most of these parameters come from instantaneous information of the flow. However, each cardiac cycle is a continuous contribution of different phases, and ten minutes of exercise is comprised of hundreds of cycles. It is difficult to evaluate the combined effect with hemodynamic parameters. Moreover, most AAAs are accompanied by mural thrombus formation that inhibits the direct contact of flow with the vessel wall, questioning the role of shear endothelium-mediated process in aneurysm progression [37]. Lagrangian analysis of flow field can use the continuous information of the flow from multiple cycles, and the LCS are tightly related to fluid forces [38]. However, it is still not clearly understood how all of these information precisely affect the progression of the

disease. This requires further investigations including tracking aneurysm progression along with correlating such results to hemodynamics data.

Acknowledgments

REFERENCES

1. Dalman R, Tedesco M, Myers J, Taylor C. AAA disease. Annals of the New York Academy of Sciences. 2006; 1085(1):92–109. [PubMed: 17182926]

2. Dua M, Dalman R. Hemodynamic influences on abdominal aortic aneurysm disease: application of biomechanics to aneurysm pathophysiology. Vascular pharmacology. 2010; 53(1):11–21. [PubMed: 20347049]

3. Yeung J, Kim H, Abbruzzese T, Vignon-Clementel I, Draney-Blomme M, Yeung K, Perkash I, Herfkens R, Taylor C, Dalman R. Aortoiliac hemodynamic and morphologic adaptation to chronic spinal cord injury. Journal of vascular surgery. 2006; 44(6):1254–1265. [PubMed: 17145427]

4. Vollmar J, Pauschinger P, Paes E, Henze E, Friesch A. Aortic aneurysms as late sequelae of above-knee amputation. The Lancet. 1989; 334(8667):834–835.

5. Taylor C, Cheng C, Espinosa L, Tang B, Parker D, Herfkens R. In vivo quantification of blood flow and wall shear stress in the human abdominal aorta during lower limb exercise. Annals of biomedical engineering. 2002; 30(3):402–408. [PubMed: 12051624]

6. Humphrey J, Taylor C. Intracranial and abdominal aortic aneurysms: similarities, differences, and need for a new class of computational models. Annual Review of Biomedical Engineering. 2008; 10:221.

7. Cheng C, Herfkens R, Taylor C. Abdominal aortic hemodynamic conditions in healthy subjects aged 50–70 at rest and during lower limb exercise: in vivo quantification using MRI. Atherosclerosis. 2003; 168(2):323–331. [PubMed: 12801616]

8. Tang B, Cheng C, Draney M, Wilson N, Tsao P, Herfkens R, Taylor C. Abdominal aortic hemodynamics in young healthy adults at rest and during lower limb exercise: quantification using image-based computer modeling. American Journal of Physiology-Heart and Circulatory Physiology. 2006; 291(2):668–676.

9. Egelhoff C, Budwig R, Elger D, Khraishi T, Johansen K. Model studies of the flow in abdominal aortic aneurysms during resting and exercise conditions. Journal of Biomechanics. 1999; 32(12): 1319–1329. [PubMed: 10569710]

10. Deplano V, Knapp Y, Bertrand E, Gaillard E. Flow behaviour in an asymmetric compliant experimental model for abdominal aortic aneurysm. Journal of Biomechanics. 2007; 40:2406–2413. [PubMed: 17258220]

11. Khanafer K, Bull J, Upchurch G, Berguer R. Turbulence significantly increases pressure and fluid shear stress in an aortic aneurysm model under resting and exercise flow conditions. Annals of vascular surgery. 2007; 21(1):67–74. [PubMed: 17349339]

12. Les A, Shadden S, Figueroa C, Park J, Tedesco M, Herfkens R, Dalman R, Taylor C. Quantification of hemodynamics in abdominal aortic aneurysms during rest and exercise using magnetic resonance imaging and computational fluid dynamics. Annals of Biomedical Engineering. 2010; 38:1288–1313. [PubMed: 20143263]

13. Suh G, Tenforde A, Shadden S, Spilker R, Cheng C, Herfkens R, Dalman R, Taylor C. Hemodynamic changes in abdominal aortic aneurysms with increasing exercise intensity using MR exercise imaging and image-based computational fluid dynamics. Annals of Biomedical Engineering. 2011; 39:2186–2202. [PubMed: 21509633]

14. Shadden S, Taylor C. Characterization of coherent structures in the cardiovascular system. Annals of Biomedical Engineering. 2008; 36:1152–1162. [PubMed: 18437573]

15. Arzani A, Shadden S. Characterization of the transport topology in patient-specific abdominal aortic aneurysm models. Physics of Fluids. 2012; 24(8):1901.

16. Mathew G, Mezi0 I, Petzold L. A multiscale measure for mixing. Physica D: Nonlinear Phenomena. 2005; 211(1):23–46.

17. Schmidt J, Delp S, Sherman M, Taylor C, Pande V, Altman R. The simbios national center: Systems biology in motion. Proceedings of the IEEE. 2008; 96(8):1266–1280. [PubMed: 20107615]

18. Taylor C, Hughes T, Zarins C. Finite element modeling of blood flow in arteries. Computer methods in applied mechanics and engineering. 1998; 158(1):155–196.

19. Jansen K, Whiting C, Hulbert G. A generalized-alpha method for integrating the filtered Navier-Stokes equations with a stabilized finite element method. Computer methods in applied mechanics and engineering. 2000; 190(3–4):305–319.

20. Vignon-Clementel I, Figueroa C, Jansen K, Taylor C. Outflow boundary conditions for three-dimensional finite element modeling of blood flow and pressure in arteries. Computer Methods in Applied Mechanics and Engineering. 2006; 195(29–32):3776–3796.

21. Moore J Jr, Ku D. Pulsatile velocity measurements in a model of the human abdominal aorta under resting conditions. Journal of biomechanical engineering. 1994; 116(3):337. [PubMed: 7799637]

22. Stergiopulos N, Meister J, Westerhof N. Simple and accurate way for estimating total and segmental arterial compliance: the pulse pressure method. Annals of biomedical engineering. 1994; 22(4):392–397. [PubMed: 7998684]

23. Montain S, Jilka S, Ehsani A, Hagberg J. Altered hemodynamics during exercise in older essential hypertensive subjects. Hypertension. 1988; 12(5):479–484. [PubMed: 3192293]

24. Shadden, S. Transport and Mixing in Laminar Flows: From Microfluidics to Oceanic Currents. Wiley-VCH Verlag GmbH & Co. KGaA; 2011. Lagrangian coherent structures.

25. Shadden S, Lekien F, Marsden J. Definition and properties of Lagrangian coherent structures from finite-time Lyapunov exponents in two-dimensional aperiodic flows. Physica D: Nonlinear Phenomena. 2005; 212(3–4):271–304.

26. Lekien F, Shadden S, Marsden J. Lagrangian coherent structures in n-dimensional systems. Journal of Mathematical Physics. 2007; 48:065 404.

27. Hathcock JJ. Flow effects on coagulation and thrombosis. Arteriosclerosis, Thrombosis, and Vascular Biology. 2006; 26(8):1729–1737.

28. Shadden SC, Astorino M, Gerbeau JF. Computational analysis of an aortic valve jet with lagrangian coherent structures. Chaos: An Interdisciplinary Journal of Nonlinear Science. 2010; 20(1):017 512.

29. Duvernois V, Marsden AL, Shadden SC. Lagrangian analysis of hemodynamics data from fsi simulation. International Journal for Numerical Methods in Biomedical Engineering. 2013; 29(4): 445–461. [PubMed: 23559551]

30. Brown R, Chua LO. Clarifying chaos: Examples and counterexamples. International Journal of Bifurcation and Chaos. 1996; 6(2):219–249.

31. Ottino, JM. Cambridge Texts in Applied Mathematics. Cambridge: Cambridge University Press; 1989. The kinematics of mixing: stretching, chaos, and transport.

32. Mathur M, Haller G, Peacock T, Ruppert-Felsot JE, Swinney HL. Uncovering the Lagrangian skeleton of turbulence. Physical Review Letters. 2007; 98(14):144 502.

33. Lekien F, Coulliette C. Chaotic stirring in quasi-turbulent flows. Philosophical Transactions: Mathematical, Physical and Engineering Sciences. 2007:3061–3084.

34. Hardman D, Semple SI, Richards JM, Hoskins PR. Comparison of patient-specific inlet boundary conditions in the numerical modelling of blood flow in abdominal aortic aneurysm disease. Int j numer method biomed eng Feb. 2013; 29(2):165–178.

35. Biasetti J, Hussain F, Gasser TC. Blood flow and coherent vortices in the normal and aneurysmatic aortas: A fluid dynamical approach to intra-luminal thrombus formation. Journal of The Royal Society Interface. 2011; 8(63):1449–1461.

36. Steinman, DA. Assumptions in modelling of large artery hemodynamics. In: Ambrosi, D.; Quarteroni, A.; Rozza, G., editors. Modeling of Physiological Flows. Vol. vol. 5. Springer Milan; 2012. p. 1-18.

37. del Álamo J, Marsden A, Lasherasa J. Recent advances in the application of computational mechanics to the diagnosis and treatment of cardiovascular disease. Revista Española de Cardiología (English Edition). 2009; 62(7):781–805.

38. Shadden S, Hendabadi S. Potential fluid mechanic pathways of platelet activation. Biomechanics and Modeling in Mechanobiology. 2013; 12(3):467–474. [PubMed: 22782543]
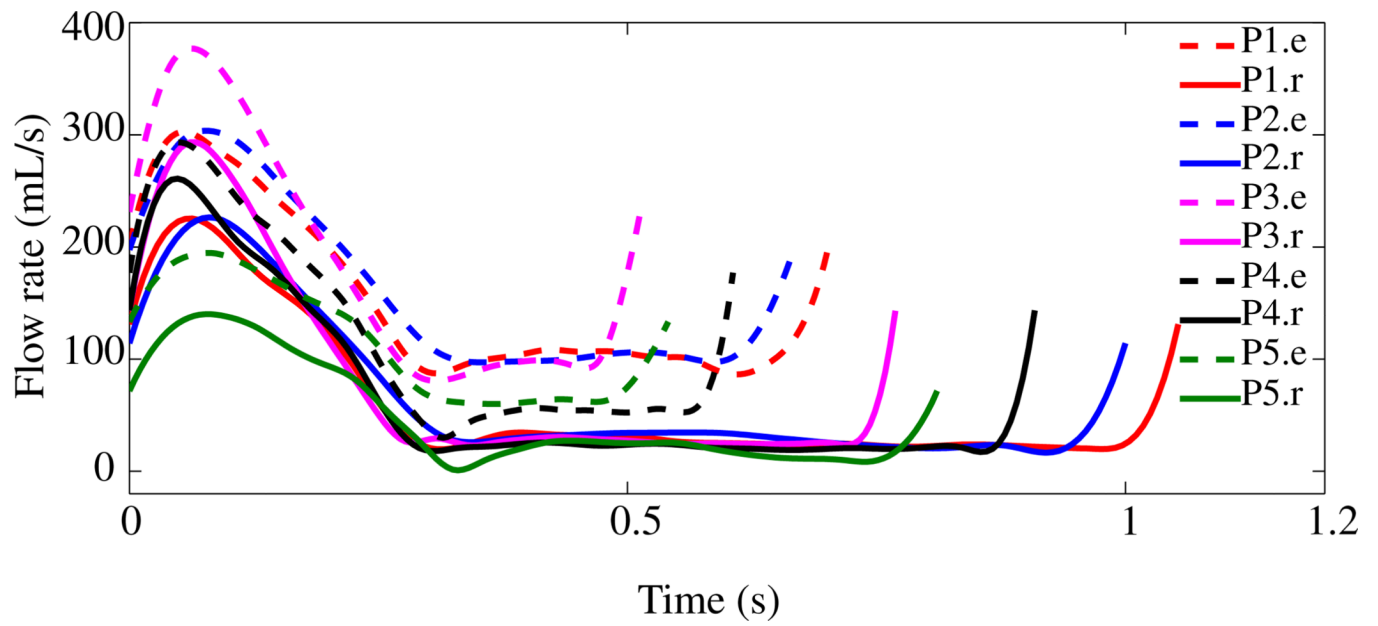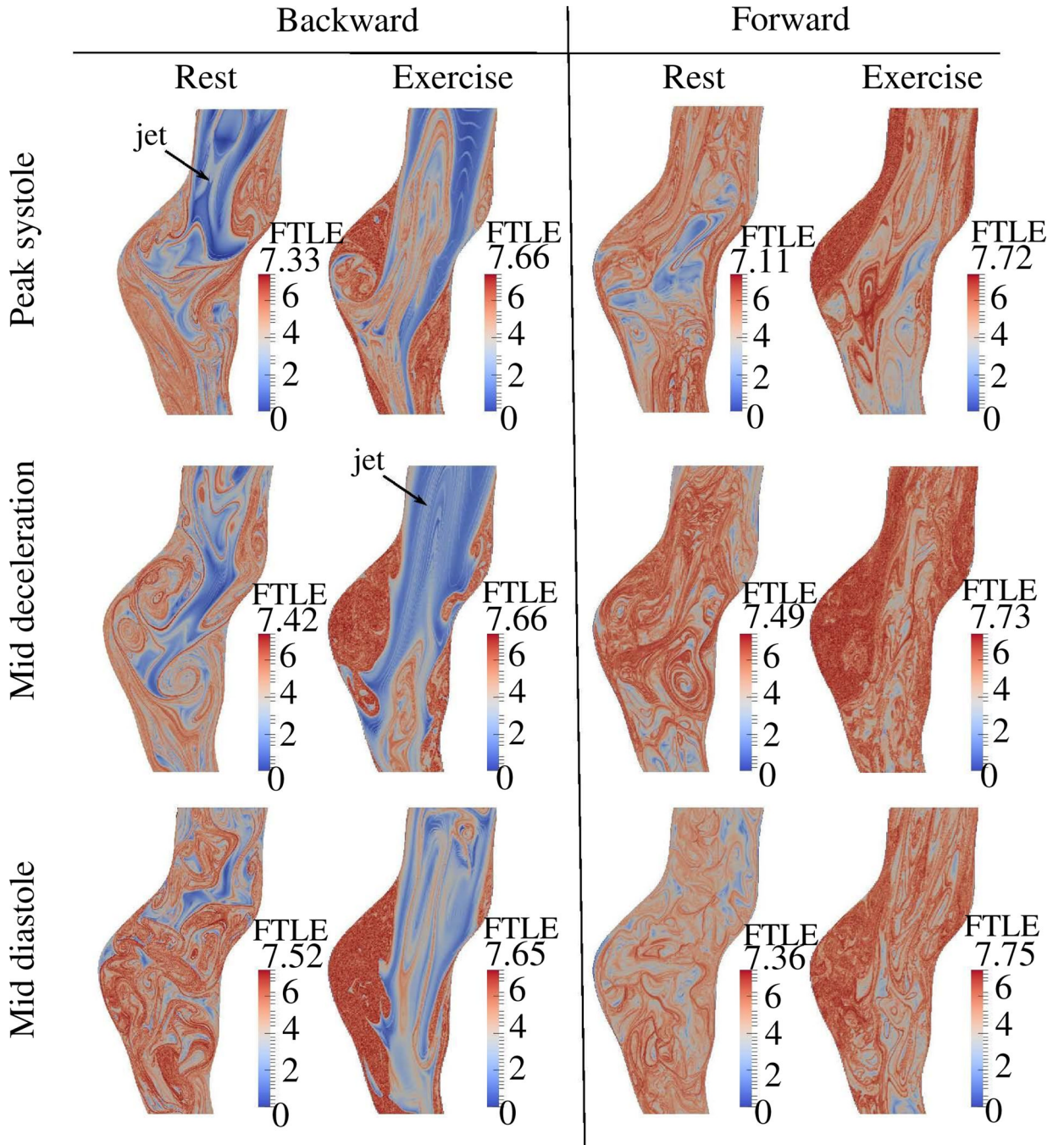
Figure 1.
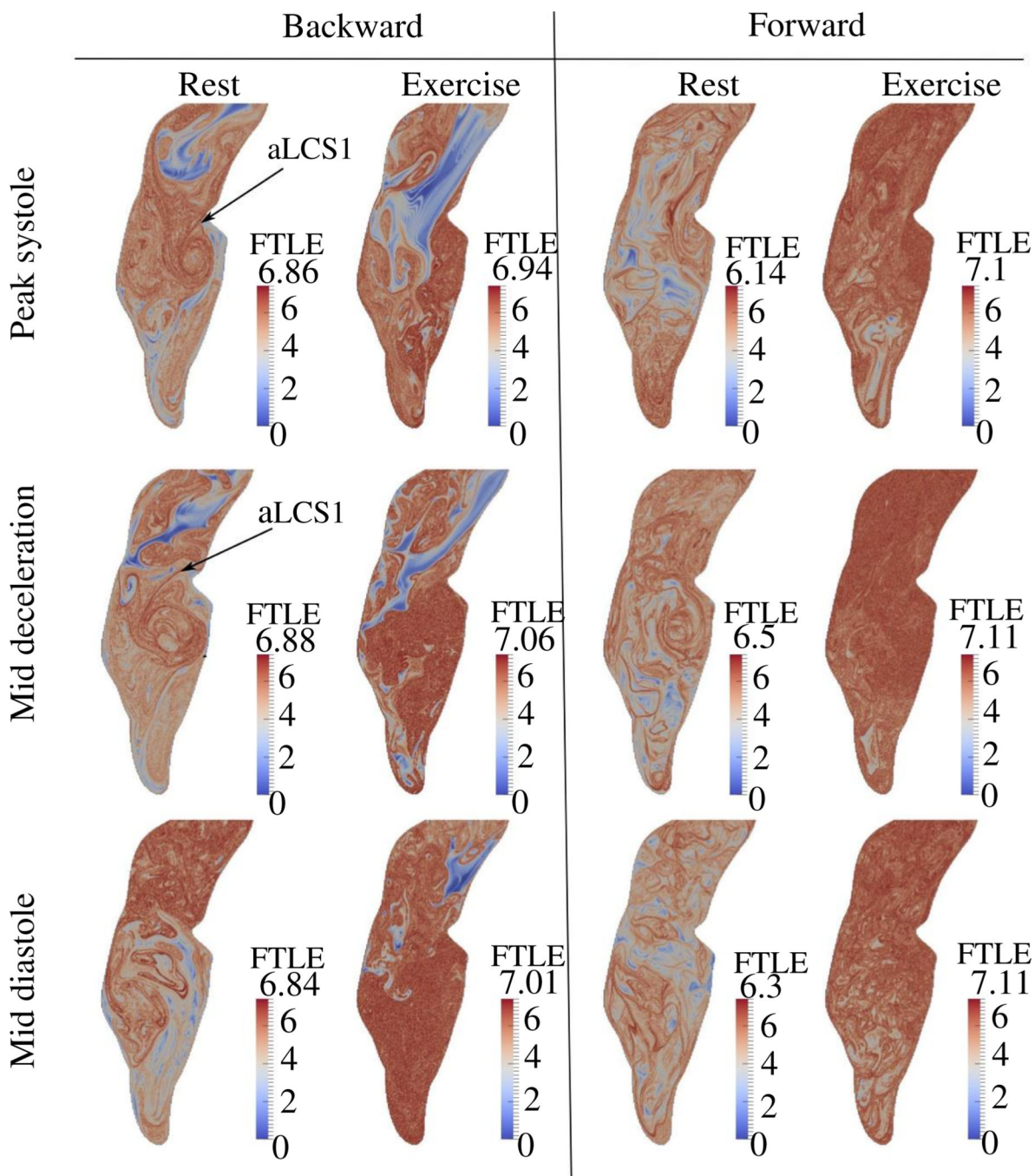Volumetric flow rates for rest and exercise used as inlet boundary condition.

Patient 1   Patient 2   Patient 3   Patient 4   Patient 5
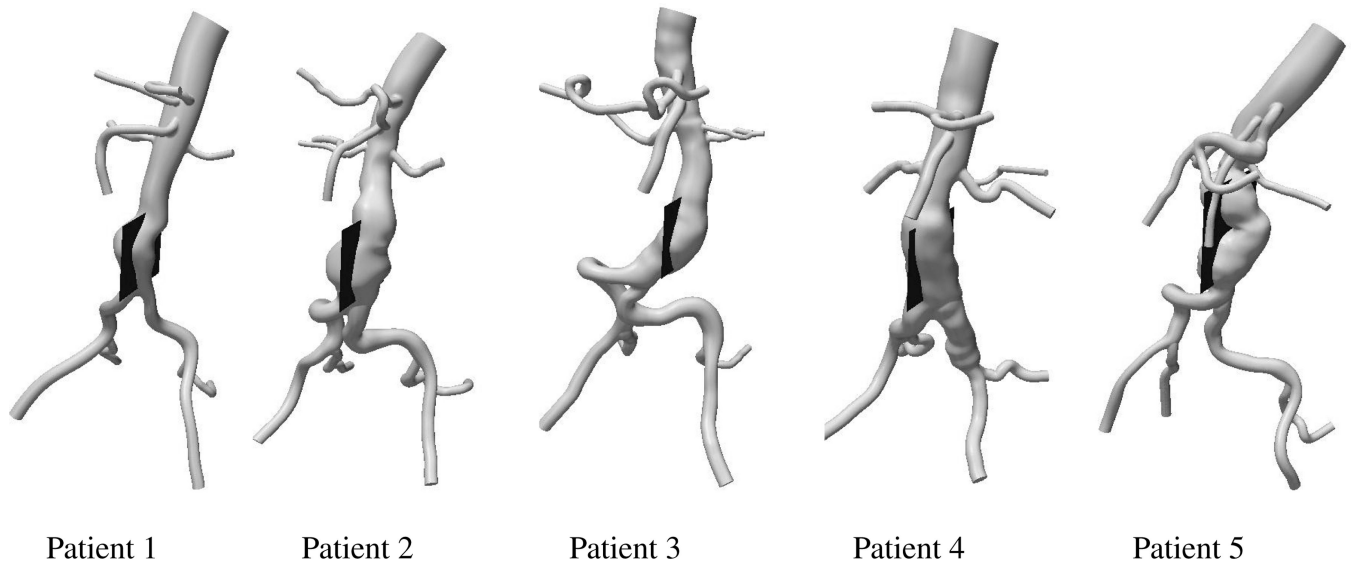
Figure 2.
AAA computer models, and the cross sections used for showing results.
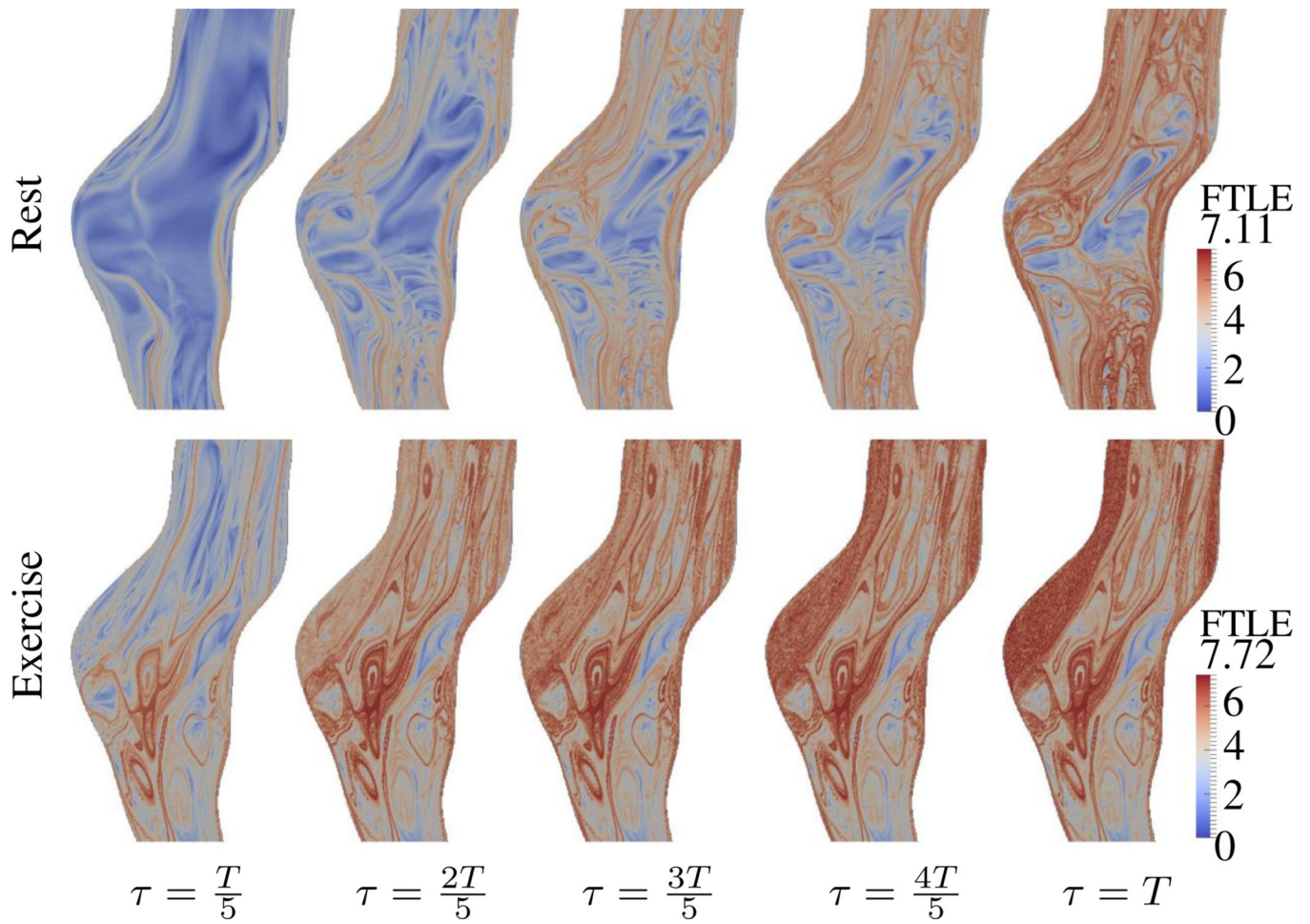
Figure 3.
Cross section view of FTLE (sagittal plane), at rest and exercise for Patient 1 at different phases of the cardiac cycle.

Figure 4.
Cross section view of FTLE (sagittal plane), at rest and exercise for Patient 2 at different phases of the cardiac cycle.
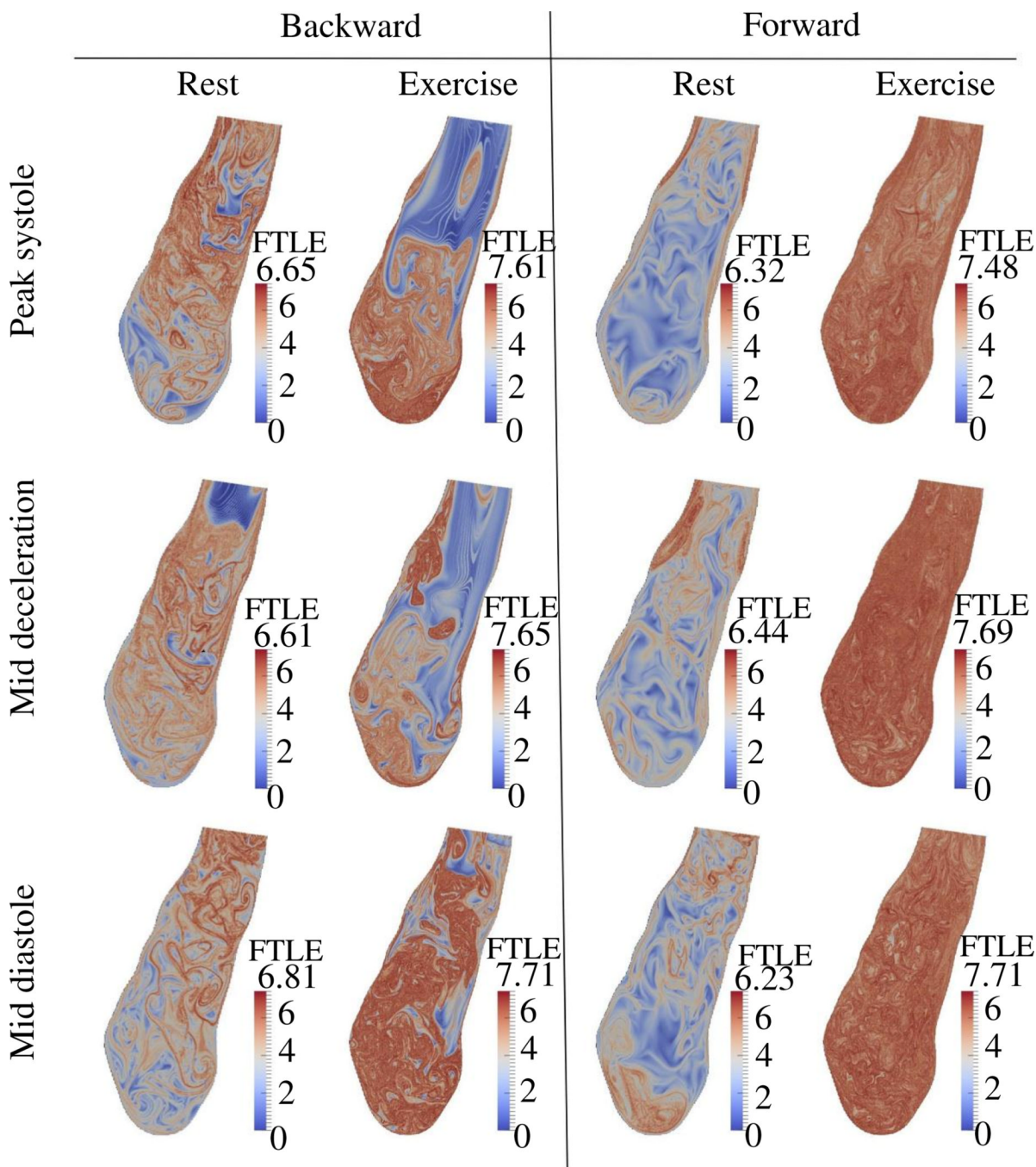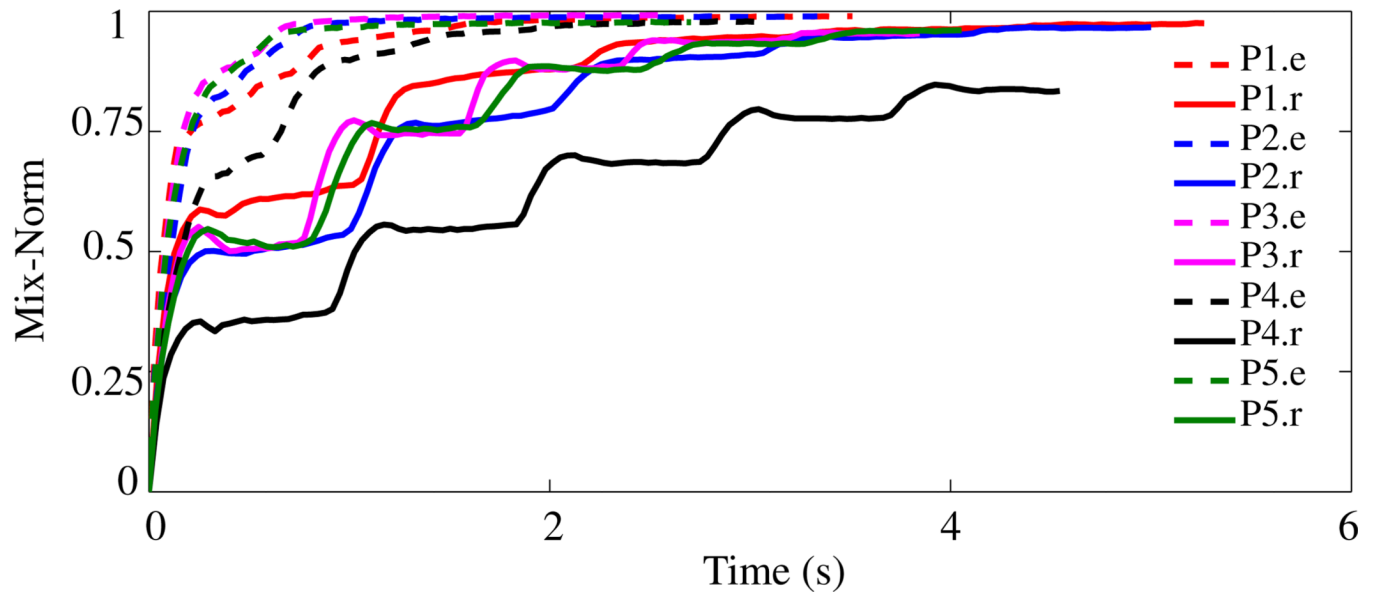
Figure 5.
Cross section view of FTLE (sagittal plane), at rest and exercise for Patient 3 at different phases of the cardiac cycle.
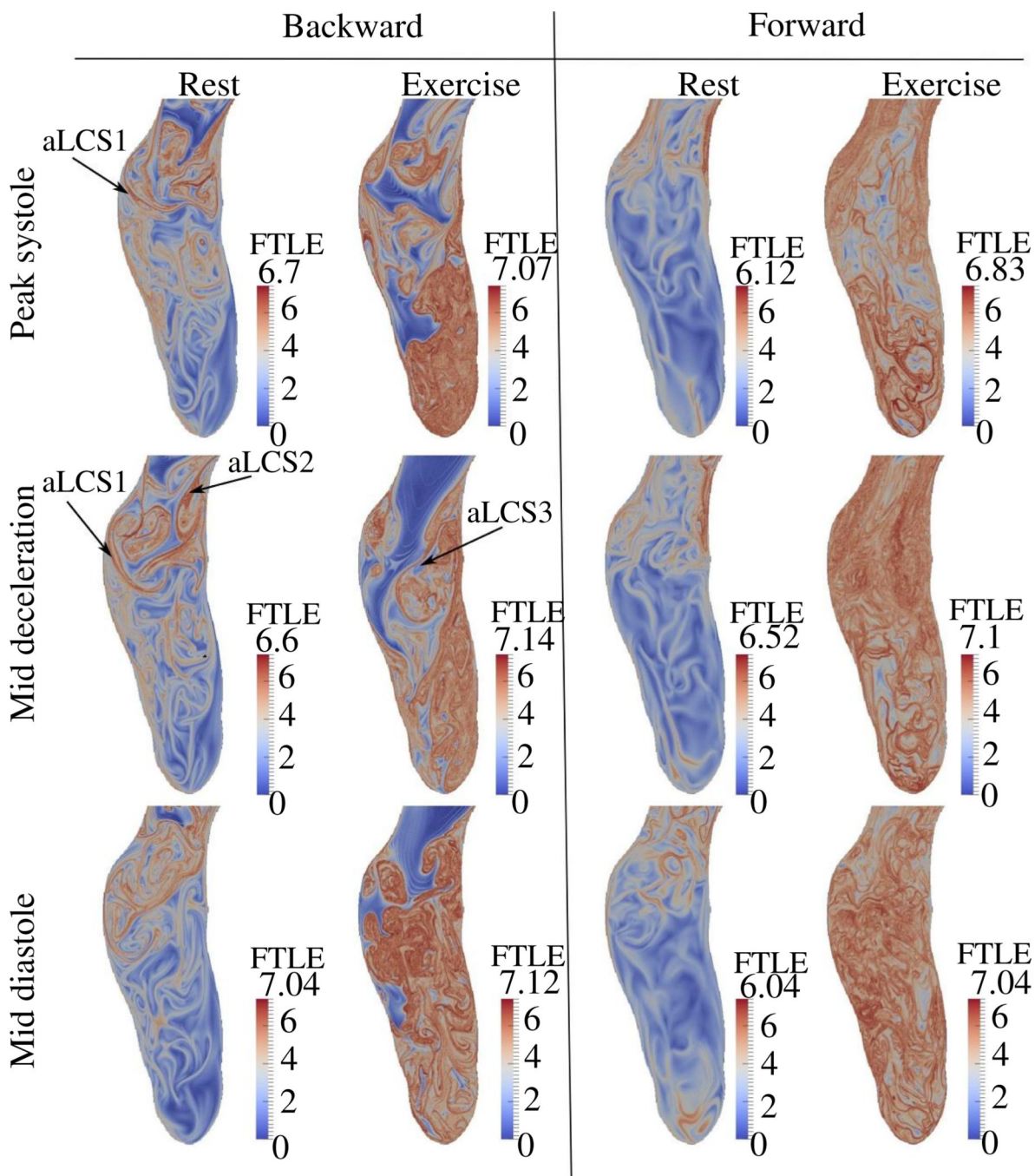
Figure 6.
Cross section view of FTLE (sagittal plane), at rest and exercise for Patient 4 at different phases of the cardiac cycle.
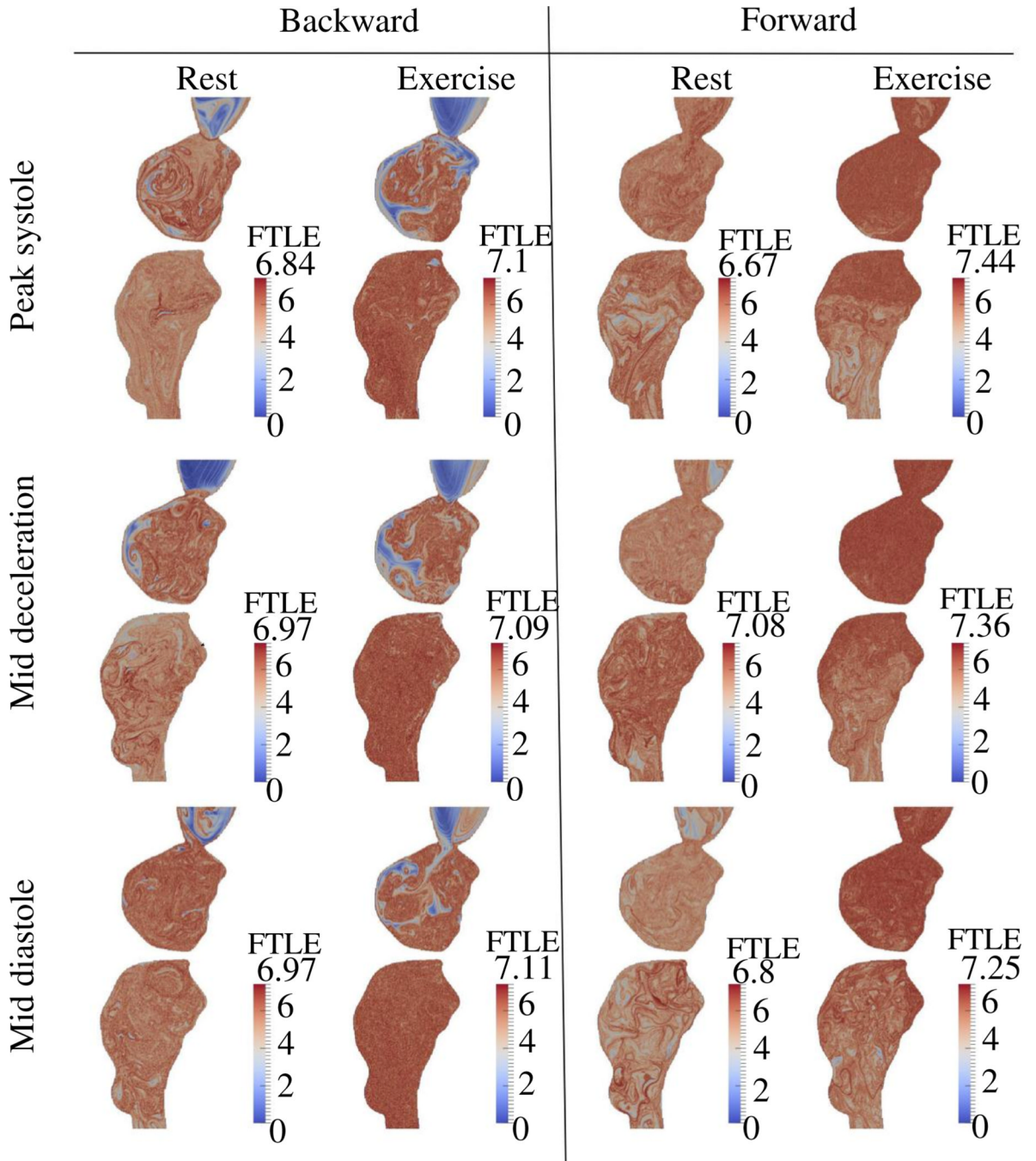
Figure 7.
Cross section view of FTLE (sagittal plane), at rest and exercise for Patient 5 at different phases of the cardiac cycle.
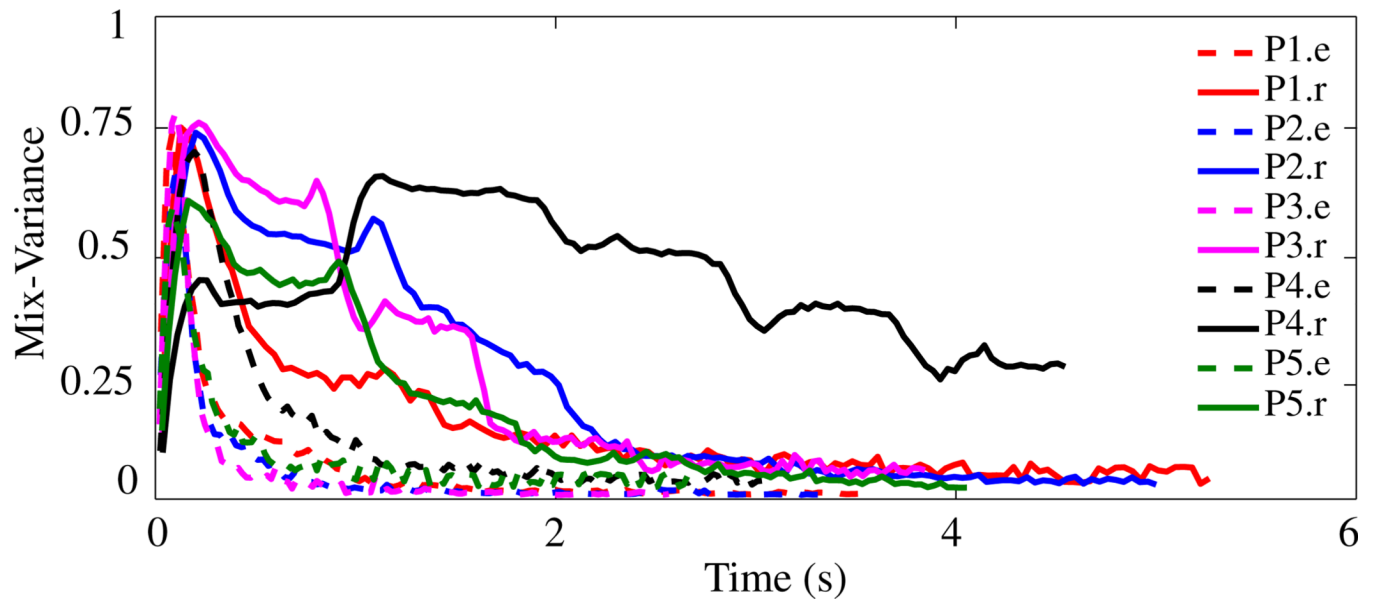
Figure 8.
Effect of integration time on forward FTLE for different choices of τ in terms of the cardiac length *T*, during peak systole.
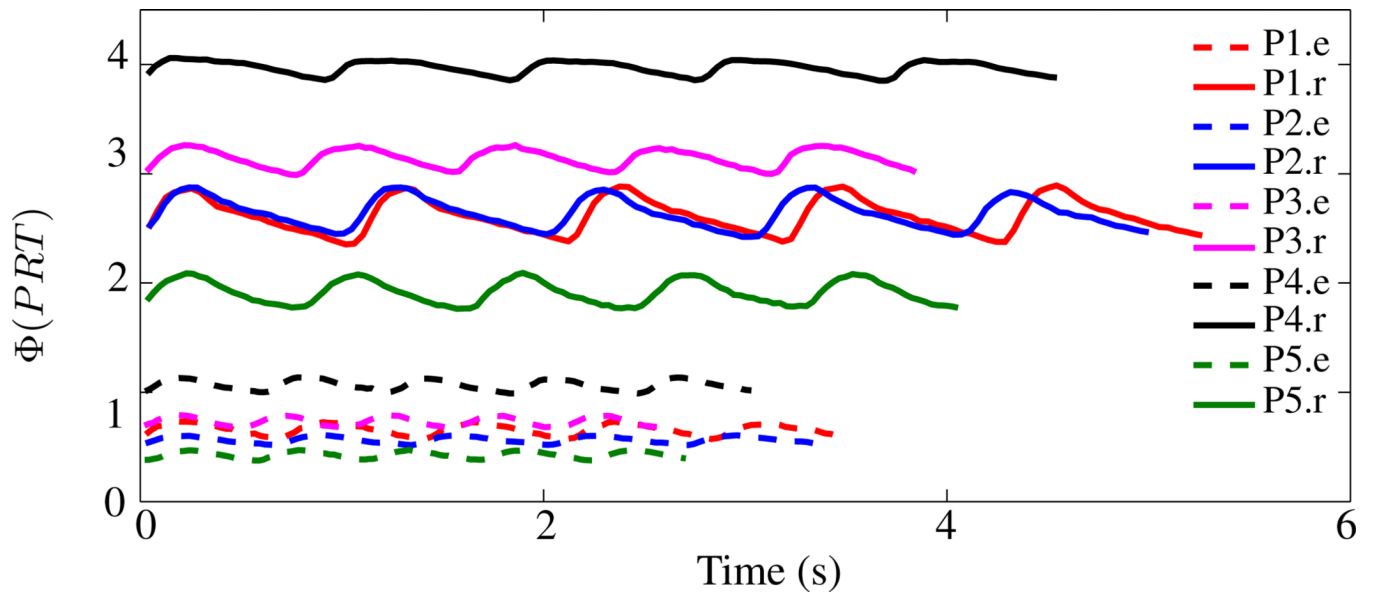
Figure 9.
Mix-norm plots for the patients during rest (r) and exercise (e). Computations are done for 5 cardiac cycles.
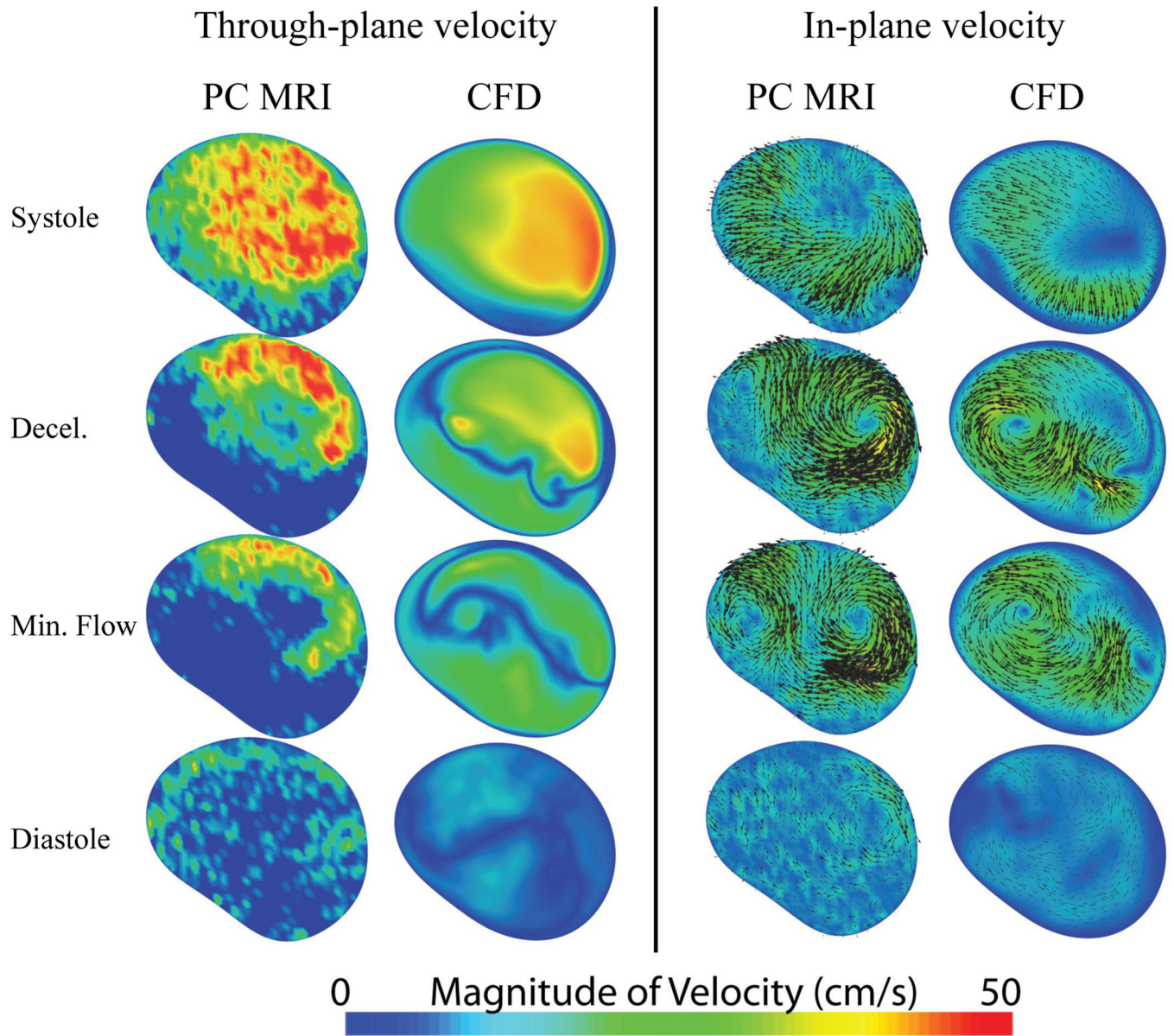
Figure 10.
Mix-variance plots for the patients during rest (r) and exercise (e). Computations are done for 5 cardiac cycles.

Figure 11.
Residence time mix-norm plots for the patients during rest (r) and exercise (e).
Computations are done for 5 cardiac cycles.

Figure 12.
Comparison of measured PCMRI velocity fields versus computed velocity fields in the mid-aneurysm of Patient 2.

Table I

Peak Reynolds number during rest and exercise

Patient #	Patient 1	Patient 2	Patient 3	Patient 4	Patient 5
Rest	2002	2241	2256	1667	1791
Exercise	4254	4552	4935	3125	3570